# Improved measurement of $^8$B solar neutrinos with 1.5 kt·y of Borexino exposure

(Borexino Collaboration)

M. Agostini,[1] K. Altenmüller,[2] S. Appel,[2] V. Atroshchenko,[3] Z. Bagdasarian,[4] D. Basilico,[5] G. Bellini,[5] J. Benziger,[6] D. Bick,[7] G. Bonfini,[8] D. Bravo,[9] B. Caccianiga,[5] F. Calaprice,[10] A. Caminata,[11] S. Caprioli,[5] M. Carlini,[8] P. Cavalcante,[12] A. Chepurnov,[13] K. Choi,[14] L. Collica,[5] D. D'Angelo,[5] S. Davini,[11] A. Derbin,[15] X.F. Ding,[1] A. Di Ludovico,[10] L. Di Noto,[11] I. Drachnev,[16] K. Fomenko,[17] A. Formozov,[18] D. Franco,[19] F. Gabriele,[8] C. Galbiati,[10] C. Ghiano,[8] M. Giammarchi,[5] A. Goretti,[10] M. Gromov,[13] D. Guffanti,[1] C. Hagner,[7] T. Houdy,[19] E. Hungerford,[20] Aldo Ianni,[8, a] Andrea Ianni,[10] A. Jany,[21] D. Jeschke,[2] V. Kobychev,[22] D. Korablev,[17] G. Korga,[20] D. Kryn,[19] M. Laubenstein,[8] E. Litvinovich,[23] F. Lombardi,[8, b] P. Lombardi,[5] L. Ludhova,[24] G. Lukyanchenko,[3] L. Lukyanchenko,[3] I. Machulin,[23] G. Manuzio,[11] S. Marcocci,[25] J. Martyn,[26] E. Meroni,[5] M. Meyer,[27] L. Miramonti,[5] M. Misiaszek,[21] V. Muratova,[15] B. Neumair,[2] L. Oberauer,[2] B. Opitz,[7] V. Orekhov,[3] F. Ortica,[28] M. Pallavicini,[11] L. Papp,[2] Ö. Penek,[24] N. Pilipenko,[15] A. Pocar,[29] A. Porcelli,[26] G. Ranucci,[5] A. Razeto,[8] A. Re,[5] M. Redchuk,[24] A. Romani,[28] R. Roncin,[30] N. Rossi,[8] S. Schönert,[2] D. Semenov,[15] M. Skorokhvatov,[23] O. Smirnov,[17] A. Sotnikov,[17] L.F.F. Stokes,[8] Y. Suvorov,[31] R. Tartaglia,[8] G. Testera,[11] J. Thurn,[27] M. Toropova,[3] E. Unzhakov,[15] A. Vishneva,[17] R.B. Vogelaar,[32] F. von Feilitzsch,[2] H. Wang,[33] S. Weinz,[26] M. Wojcik,[21] M. Wurm,[26] Z. Yokley,[32] O. Zaimidoroga,[17] S. Zavatarelli,[11] K. Zuber,[27] and G. Zuzel[21]

[1] *Gran Sasso Science Institute (INFN), 67100 L'Aquila, Italy*
[2] *Physik-Department and Excellence Cluster Universe, Technische Universität München, 85748 Garching, Germany*
[3] *National Research Centre Kurchatov Institute, 123182 Moscow, Russia*
[4] *IKP-2 Forschungzentrum Jülich, 52428 Jülich, Germany*
[5] *Dipartimento di Fisica, Università degli Studi e INFN, 20133 Milano, Italy*
[6] *Chemical Engineering Department, Princeton University, Princeton, NJ 08544, USA*
[7] *Institut für Experimentalphysik, Universität Hamburg, 22761 Hamburg, Germany*
[8] *INFN Laboratori Nazionali del Gran Sasso, 67010 Assergi (AQ), Italy*
[9] *Physics Department, Virginia Polytechnic Institute and State University, Blacksburg, VA 24061, USA,Milano*
[10] *Physics Department, Princeton University, Princeton, NJ 08544, USA*
[11] *Dipartimento di Fisica, Università degli Studi e INFN, 16146 Genova, Italy*
[12] *INFN Laboratori Nazionali del Gran Sasso, 67010 Assergi (AQ), Italy,Virginia*
[13] *Lomonosov Moscow State University Skobeltsyn Institute of Nuclear Physics, 119234 Moscow, Russia*
[14] *Department of Physics and Astronomy, University of Hawaii, Honolulu, HI 96822, USA*
[15] *St. Petersburg Nuclear Physics Institute NRC Kurchatov Institute, 188350 Gatchina, Russia*
[16] *Gran Sasso Science Institute (INFN), 67100 L'Aquila, Italy,Peters*
[17] *Joint Institute for Nuclear Research, 141980 Dubna, Russia*
[18] *Joint Institute for Nuclear Research, 141980 Dubna, Russia,Milano,Lomonosov*
[19] *AstroParticule et Cosmologie, Université Paris Diderot, CNRS/IN2P3, CEA/IRFU, Observatoire de Paris, Sorbonne Paris Cité, 75205 Paris Cedex 13, France*
[20] *Department of Physics, University of Houston, Houston, TX 77204, USA*
[21] *M. Smoluchowski Institute of Physics, Jagiellonian University, 30059 Krakow, Poland*
[22] *Kiev Institute for Nuclear Research, 03680 Kiev, Ukraine*
[23] *National Research Centre Kurchatov Institute, 123182 Moscow, Russia,Kurchatovb*
[24] *IKP-2 Forschungzentrum Jülich, 52428 Jülich, Germany,RWTH*
[25] *Gran Sasso Science Institute (INFN), 67100 L'Aquila, Italy,Genova*
[26] *Institute of Physics and Excellence Cluster PRISMA, Johannes Gutenberg-Universität Mainz, 55099 Mainz, Germany*
[27] *Department of Physics, Technische Universität Dresden, 01062 Dresden, Germany*
[28] *Dipartimento di Chimica, Biologia e Biotecnologie, Università degli Studi e INFN, 06123 Perugia, Italy*
[29] *Amherst Center for Fundamental Interactions and Physics Department, University of Massachusetts, Amherst, MA 01003, USA*
[30] *INFN Laboratori Nazionali del Gran Sasso, 67010 Assergi (AQ), Italy,APC*
[31] *Physics and Astronomy Department, University of California Los Angeles (UCLA), Los Angeles, California 90095, USA,Kurchatov*
[32] *Physics Department, Virginia Polytechnic Institute and State University, Blacksburg, VA 24061, USA*
[33] *Physics and Astronomy Department, University of California Los Angeles (UCLA), Los Angeles, California 90095, USA*

(Dated: November 6, 2023)

We report on an improved measurement of the $^8$B solar neutrino interaction rate with the Borexino detector at the Laboratori Nazionali del Gran Sasso. Neutrinos are detected via their elastic scattering on electrons in a large, radio-pure liquid scintillator target. Novel analysis approaches exploiting most of the active volume of the detector have enabled the collection of data from 1.5 kt·y exposure between 2008 and 2016. The measured rate of solar neutrino-induced, scattered electrons above 3 MeV of energy is $0.220^{+0.015}_{-0.016}\,(stat)\,^{+0.006}_{-0.006}\,(syst)$ cpd/100 t, which corresponds to an observed solar

neutrino flux assuming no neutrino flavor conversion of $2.55^{+0.17}_{-0.19}(stat)^{+0.07}_{-0.07}(syst)\times10^6$ cm$^{-2}$ s$^{-1}$. If one assumes the $^8$B solar neutrino flux predicted by the high metallicity Standard Solar Model, the average $^8$B solar $\nu_e$ survival probability is 0.36±0.08 at the mean visible energy of 7.9 MeV, in good agreement with the MSW-LMA scenario.

## I. INTRODUCTION

The observation of lepton flavor transformation of solar neutrinos has played a decisive role in uncovering the phenomenon of neutrino oscillations [1–7]. Solar neutrino flavor conversion is well described by the Mikheyev-Smirnov-Wolfenstein (MSW) mechanism in matter and neutrino mixing [8, 9]. Uncontroversial experimental evidence that neutrinos oscillate exists for atmospheric neutrinos [10], as well as neutrinos produced at accelerators [11] and nuclear reactors [12]. However, while reactor anti-neutrino oscillations at the L/E solar frequency, where L is the distance traveled and E is the neutrino energy, have been clearly established by KamLAND [13], a definitive experimental signature of solar neutrino flavor conversion able to completely rule out other non-standard conversion mechanisms is still missing.

Predicted signatures of MSW-LMA solar neutrino oscillations include the observation of MSW electron neutrino regeneration of solar neutrinos traversing the Earth (the so-called *day-night* effect), and a characteristic turn-up of the electron neutrino survival probability below 3 MeV. A first evidence of day-night asymmetry of the $^8$B solar neutrino rate was recently reported by Super-Kamiokande [14]. The transition region for electron solar neutrino survival probability continues to elude direct experimental investigation. Thus the study of $^8$B solar neutrinos with low energy threshold (alongside that of CNO neutrinos) is important to test fundamental properties of neutrinos as well as the detailed workings of solar fusion.

Borexino detects solar neutrinos with the lowest energy threshold of all solar neutrino experiments to date. It has measured, in order of increasing energy, the *pp*, $^7$Be, and *pep* neutrino interaction rates [15–18], and the $^8$B neutrino interaction rate of neutrinos above ∼3 MeV [19]. The measured electron flavor survival probability of solar neutrinos is fully compatible with the MSW-LMA neutrino oscillation picture by which low energy *pp*, $^7$Be, and *pep* neutrinos undergo *vacuum oscillations* and $^8$B experience enhanced MSW resonant *matter* conversion.

Borexino detects solar neutrinos via $\nu - e$ elastic scattering in liquid scintillator. The 3 MeV electron recoil threshold used in this study approaches (from above) the yet unexplored energy region where MSW predicts the *matter-to-vacuum oscillation* electron survival probability upturn to occur. Available low-threshold measurements by Borexino [19] and SNO [20] might suggest a deviation from this prediction, although with limited discriminating power. Exploring this region is hence of great interest because of the sensitivity to new physics, including non-standard neutrino interactions [21] and light sterile neutrinos [22, 23].

This work is also motivated by solar physics. The simultaneous, precise measurement of the $^7$Be and $^8$B solar neutrino interaction rates is a robust test of the Standard Solar Model (SSM) [24] by informing on the metal composition of the Sun, whose uncertainty is currently at the center of a lively debate [25]. The conflict arises over a recent determination of solar metal abundances (referred to as "low-Z") obtained from a sophisticated 3D modeling of the solar photospheric spectrum [26]. These models predict a metal content of the Sun ∼2 times smaller than previous "high-Z" models [27], resulting from a mono-dimensional approach. Despite the 3D model strongly improves the agreement with the surface granularity, the width, shift, and asymmetries of spectral lines, a significant discrepancy appears between low-Z SSM predictions and helioseismological measurements.

The low-Z model predicts reduced $^7$Be and $^8$B solar neutrino fluxes, down ∼9% and ∼19% from high-Z values, respectively, and essentially unchanged *pp* and *pep* fluxes [24]. Despite large theoretical uncertainties on the SSM $^7$Be and $^8$B fluxes (6% and 12%, respectively), their precise measurement could discriminate between high and low solar metallicity models.

Borexino has recently improved the measurements of *pp*, *pep*, and $^7$Be interaction rates, the latter reaching a precision of better than 3% [28]. Here we present an improved measurement of the $^8$B solar neutrino interaction rate, with more than a 10-fold increase of exposure with respect to the previous measurement [19]. In addition to a longer data acquisition period, this was enabled by a much-enlarged fiducial mass encompassing almost the entire Borexino 278 t scintillator target. This analysis preserves the electron energy threshold at ∼3 MeV. Other notable improvements include the reduction of radioactive backgrounds following the 2011 scintillator purification campaign, effective at strongly reducing the $^{208}$Tl contamination, and a new multi-variate approach to constrain the cosmogenic $^{11}$Be contamination. Finally, we identified a new source of background induced by radiogenic neutrons, not considered by the previous analysis.

## II. EXPERIMENTAL APPARATUS

Borexino is located underground in the Laboratori Nazionali del Gran Sasso (LNGS) in central Italy at a depth of 3800 m.w.e. Neutrinos are detected via elastic scattering on electrons in a 278 t (nominally) organic liq-

[a] Also at: Laboratorio Subterráneo de Canfranc, Paseo de los Ayerbe S/N, 22880 Canfranc Estacion Huesca, Spain
[b] Present address: Physics Department, University of California, San Diego, CA 92093, USA

uid scintillator target. The scintillator consists of pseudocumene solvent (PC, 1,2,4-trimethylbenzene) doped with 1.5 g/l of PPO (2,5-diphenyloxazole), a fluorescent dye. The liquid scintillator is contained in a 125 $\mu$m-thick, spherical nylon vessel of 4.25 m nominal radius. Scintillation light is detected by 2212 ETL 9351 8" photomultiplier tubes (PMTs) uniformly mounted on a 13.7 m-diameter stainless steel sphere (SSS). Two concentric spherical buffer shells separate the active scintillator from the PMTs and SSS (323 t and 567 t, respectively). They are filled with PC doped with dimethyl phthalate (DMP) to quench unwanted peripheral scintillation and shield the central active target from radiation emitted by the PMTs and SSS. The two PC buffers are separated by a second 125 $\mu$m-thick nylon membrane that prevents the diffusion of radon emanated by the PMTs and by the SSS into the central scintillator volume. Everything inside the SSS constitutes the inner detector (ID).

The SSS is surrounded by a domed, cylindrical water tank (18.0 m diameter, 16.9 m height), containing 2100 t of ultra-pure water and serving as an additional absorber for external $\gamma$-rays and neutrons from the laboratory cavern. The water tank is equipped with 208 8" PMTs, and run as a Čerenkov detector (and veto) of cosmic muons (outer detector, OD [29]). A complete description of the Borexino detector can be found in [30].

## III. DETECTOR RESPONSE

The modeling of the Borexino detector response has been steadily improving since the beginning of data-taking in 2007. Invaluable information has been provided by an extensive calibration campaign in 2009 [31]. Moreover, the large body of data recorded over a decade has enabled extensive optimization of the Monte Carlo simulation of the detector [32]. The level of understanding of the Borexino apparatus has enabled us to extend the $^8$B neutrino analysis to the entire scintillator target, an almost 3-fold increase from the previous measurement [19].

The adopted analysis provides handles to reject most of the background components on an event-by-event basis via specific selection cuts (Section IV). The radial distribution of the events surviving these cuts is fitted to discriminate bulk events occurring inside the scintillator volume (including solar neutrino events) from backgrounds originating outside the scintillator (see Sections V and VI). No assumption is made on the neutrino energy spectrum, which allows us to test for any deviation from the MSW prediction. An accurate monitoring of the time evolution of the detector response is necessary. An important example is offered by the monitoring of a scintillator leak into the buffer region, started in April 2008, which caused the scintillator nylon vessel to deform over time. This effect is amplified by the mixing due to convective currents induced by temperature variations in the detector hall. Another important time-dependent effect to consider is the occasional loss of PMTs and the variation of their performance over the years.

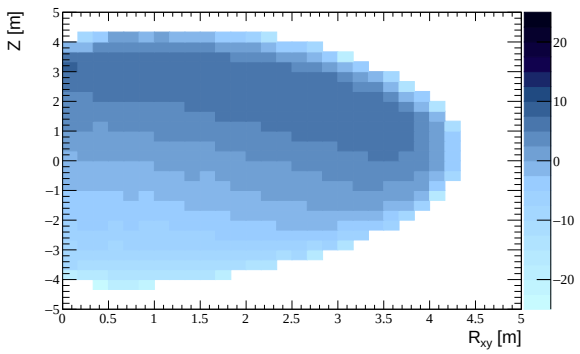


FIG. 1. Relative variation [%], from Monte Carlo simulations, of the light yield with respect to the detector center, as function of the event reconstructed position (z vs $R_{xy}=\sqrt{x^2+y^2}$). The correspondent systematic error was estimated in $\sigma$=1.9%, using $^{241}$Am-$^9$Be calibration data.

To appropriately model time-dependent effects, we generate Monte Carlo simulated data sets on a weekly basis, which incorporate an exact map of operating PMT's and their performance parameters (such as gain and noise) determined with periodic laser calibration runs. In addition, the time-varying profile of the scintillator vessel shape is also included and updated every week. It is measured by locating background events generated by trace radioactive contamination embedded in the nylon film. The uncertainty on the reconstructed radial position of the nylon vessel is estimated at 1% by comparing the reconstructed position of background events with the position of the membrane extracted from pictures taken with CCD cameras [18, 31]. Weekly simulated data sets contain $10^2$–$10^3$ times events than the real data and are collated after weighting them by the detector live time. This procedure applied to all the simulations used in this work, unless otherwise stated.

The energy threshold for this analysis is set at 3.2 MeV equivalent electron energy, with 50% detection efficiency, to entirely reject 2.614 MeV $\gamma$-rays from $^{208}$Tl, due to $^{232}$Th contamination in the PMT's and the SSS. The energy calibration relies on the characteristic $\gamma$ transitions from neutron captures on hydrogen and carbon, of 2.22 MeV and 4.95 MeV, respectively. Neutrons are emitted by a $^{241}$Am-$^9$Be source inserted in the scintillator. The light yield is defined as the sum of the integrated charge measured by each PMT and is expressed in photoelectrons (pe). In the central region of the detector (R<1 m) it is ∼500 pe/MeV/2000 PMT's: the Monte Carlo model reproduces it to within 1% [31, 32].

The non-uniformity of the spatial distribution of working PMTs, together with the scintillator light attenuation causes the energy response to depend on the event position. The Monte Carlo model predicts a relative variation of the light yield with respect to the center that ranges from -23% in the bottom hemisphere to +8% in the upper

hemisphere (see Figure 1).

The energy response of the model was validated by comparing data collected with the $^{241}$Am-$^{9}$Be calibration source with simulations: the relative difference of the light yield, $\Delta$LY, varies with radius up to a few % at the edge of the scintillator volume. The associated uncertainty is 1.6% when computes as the RMS of the $\Delta$LY distribution, weighted by the event density. The overall error on the Monte Carlo energy response is equal to 1.9%, which combines the uncertainties on the absolute light yield at the detector center and the relative, position-dependent variation.

The energy threshold for the analysis is set at 1650 p.e., corresponding to 3.2 MeV electron energy, with detection efficiency of 50% in the whole volume, as shown in Figure 2. The threshold is higher than the one used in our previous analysis (1494 p.e.) to take into account the higher light collection efficiency for events at high radius in the upper hemisphere, as illustrated in Figure 1. This region was previously excluded by a volume cut at 3 m radius. The upper limit is set at 8500 p.e. ($\sim$17 MeV electron energy), to fully accept $^{8}$B neutrino-induced recoil electrons.

Radial fits to the energy spectra in two sub-ranges are independently performed. A low energy range (LE), with [1650, 2950] p.e., including events from natural radioactivity, and a high energy range (HE), with [2950, 8500] p.e., dominated by external $\gamma$-rays following neutron capture processes on the SSS, as discussed in Sections IV and V. In Borexino, the energy deposited by natural, long-lived radioactivity never exceeds 5 MeV (the Q-value of the $\beta$-decay of $^{208}$Tl), since the scintillation signal from $\alpha$'s of higher kinetic energy are quenched and fall below the analysis threshold. Of the residual backgrounds surviving selection cuts (see Section IV) only cosmogenic $^{11}$Be and $\gamma$'s from neutron capture reactions make it into both energy windows. The signal detection efficiency associated to the energy cuts is evaluated by simulating neutrino events distributed uniformly throughout the active volume. The fractional number of events selected within the LE and HE ranges, converted to the recoil electron energy scale, is shown in Figure 2.

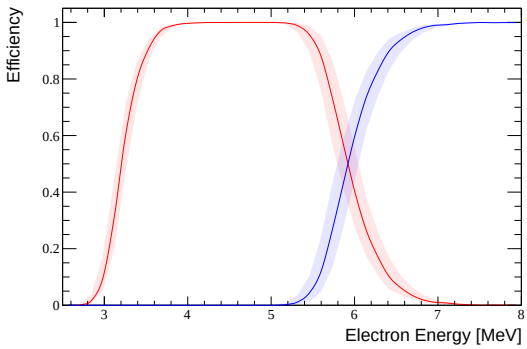


FIG. 2. Detection efficiencies and associated uncertainties (due to the electron energy scale determination) of the LE ([1650, 2950] p.e., red line) and HE ([2950, 8500] p.e., blue line) ranges as a function of electron energy. The detection efficiency equals 1 up to the 8500 p.e. upper edge of the HE range.

## IV. DATA SELECTION

This work is based on data collected between January 2008 and December 2016 and corresponds to 2062.4 live days of data, inclusive of the 388.6 live days of data used in the previous measurement. Data collected during detector operations such as scintillator purification and calibrations are omitted.

Results from the HE sample use data from the entire active volume, while the LE sample requires a spatial cut to remove the top layer of scintillator. This is motivated by the presence of PPO from the scintillator leak in the upper buffer fluid volume, which may cause events from this region to be reconstructed with energy at $\sim$3 MeV threshold. The z-cut to remove leak-related events was conservatively set at 2.5 m. The impact of this cut is investigated as a potential source of systematic uncertainty (see Section VI).

The active mass is evaluated with a toy Monte Carlo approach, by measuring the fraction of events falling within the scintillator volume for a set generated in a volume that includes it. The time-averaged mass is 266.0$\pm$5.3 ton, and assumes a scintillator density of 0.8802 g/cm$^3$ [18]. The total exposure is 1,519 t·y, a $\sim$11.5-fold increase with respect to our previous analysis. The mass fraction for the LE sample, after the z-cut at 2.5 m is 0.857$\pm$0.006, obtained using a full optical simulation that includes effects from the spatial reconstruction of events.

Data are selected with the following cuts, already discussed in reference [19]:

- *neutron cut*: a 2 ms veto is applied after each muon detected by both ID and OD, to remove cosmogenic neutron captures on carbon in the scintillator and in the buffer;
- *fast cosmogenics cut*: a 6.5 s veto is applied after each muon crossing the scintillator to remove cosmogenic isotopes with life times between a few ms and 1.2 s ($^{12}$B, $^{8}$He, $^{9}$C, $^{9}$Li, $^{8}$B, $^{6}$He, and $^{7}$Li);
- *run start/break cut*: a 6.5 s veto is applied at the beginning of each run to remove fast cosmogenic activity from muons missed during run restart;
- $^{10}$*C cut*: a spherical volume of 0.8 m radius around all muon-induced neutron captures is vetoed for 120 s to reject cosmogenic $^{10}$C ($\tau$=27.8 s);
- $^{214}$*Bi-Po cut*: $^{214}$Bi and $^{214}$Po delayed coincident decays ($^{214}$Po-$\tau$=236 $\mu$s) are identified and rejected with $\sim$100% efficiency.

Muons crossing the water tank but not the SSS (*external muons*) are detected by the OD with an efficiency >99.25% [29]. Muons crossing the scintillator (*internal muons*) are defined either by looking at simultaneous signals from the ID and OD or by looking at the scintillation pulse shape in the ID alone. The pulse shape selection variables are the mean and peak times of the scintillation time profile. An event is identified as an internal muon if the mean time of the scintillation is >100 ns or the peak time is >30 ns. The rate of residual muons contaminating the LE and HE samples are measured following the procedure described in [19] as $(1.2\pm0.1)\times10^{-4}$ and $(3.8\pm0.3)\times10^{-4}$ cpd/100 ton, respectively.

The definition of internal muon adopted by the *fast cosmogenic cut* additionally requires E>400 p.e. (∼0.8 MeV) in order to contain the dead time introduced by the *fast cosmogenic cut* itself. The energy cut has virtually no impact on the rejection efficiency of cosmogenic background, since it only removes muons that traverse 10-20 cm of buffer liquid and are hence far away from the scintillator target. The internal muon tagging inefficiency introduced by this tighter cut is $<8\times10^{-5}$ [29].

The rate of 4.95 MeV $\gamma$-rays from cosmogenic neutron captures on carbon, surviving the *neutron cut*, is $(0.72\pm0.02)\times10^{-4}$ cpd/100 t, with a mean capture time of ∼254.5 $\mu$s [29], a cosmogenic neutron rate of 90.2±3.1 cpd/100 t and the carbon-to-hydrogen neutron cross section ratio of ∼1% [33].

The residual rate of fast cosmogenics after the *fast cosmogenic cut* is $(2.4\pm0.1)\times10^{-3}$ cpd/100 t, obtained by fitting the distribution of elapsed time between each event and the previous muon (see [19] for details).

The residual contamination of $^{10}$C surviving the *$^{10}C$ cut*, is evaluated as in [19, 33]. The *$^{10}C$ cut* is effective only on "visible" reaction channels, *i.e.* those for which at least one neutron is emitted in association with $^{10}$C production. The selection efficiency is $0.925^{+0.075}_{-0.200}$ [33] and the "visible" $^{10}$C rate is found to be $0.48^{+0.04}_{-0.11}$ cpd/100 t, in good agreement with the previous measurement ($0.52^{+0.13}_{-0.09}$ cpd/100 t [33]). The residual rate from visible channels is $4.8^{+0.4}_{-1.0}\times10^{-4}$ cpd/100 ton, which includes events surviving the *$^{10}C$ cut*, the energy cut, which rejects 98.3% of $^{10}$C events, and the *fast cosmogenic* cut, with an additional 17% rejection efficiency. The residual rate from invisible production channels, dominated by the $^{12}$C(p,t)$^{10}$C reaction and evaluated in [19], is $(4.7\pm14.1)\times10^{-4}$ cpd/100 t, after *energy* and *fast cosmogenic* cuts.

The *$^{214}$Bi-Po cut* identifies $^{214}$Bi events correlated in time and space with the $^{214}$Po daughter nucleus. The closely-occurring events are searched in a [0.02, 1.4] ms time window and with a maximum separation of 1 m. In addition, we require that the Gatti parameter, an $\alpha/\beta$ pulse shape discrimination estimator [34], for the $^{214}$Po to be >-0.008. The overall efficiency of this cut is 0.91 [19]. The fraction of $^{214}$Bi with energy larger than the lower 1650 p.e. analysis threshold is derived directly from this rejected sample and is $6\times10^{-4}$. The residual $^{214}$Bi rate leaking into the LE energy window is thus $(2.2\pm1.0)\times10^{-4}$ cpd/100 t.

TABLE I. Residual background rates, after selection cuts, in the LE [1650, 2950] p.e. and HE [2950, 8000] p.e. ranges, as discussed in Section IV. The particular case of $^{11}$Be is discussed in Section V.

| Background | LE rate [$10^{-4}$ cpd/100 t] | HE rate [$10^{-4}$ cpd/100 t] |
|---|---|---|
| Fast cosmogenics | 13.6±0.6 | 10.4±0.4 |
| Muons | 1.2±0.1 | 3.8±0.3 |
| Neutrons | 0.72±0.02 | 0 |
| $^{10}$C | 9.5±14.1 | 0 |
| $^{11}$Be | $0^{+36.3}_{-0.0}$ | $0^{+54.9}_{-0.0}$ |
| $^{214}$Bi | 2.2±1.0 | 0 |
| Total | $27.2^{+38.9}_{-14.1}$ | $14.2^{+54.9}_{-0.5}$ |

The dead time introduced by all cuts is estimated with the toy Monte Carlo method. The selection cuts depend on internal and external muons and neutrons, so we generate artificial events with a constant rate (1.2 Hz) uniformly distributed in the IV and we add muon and neutron events selected from data with their time stamp. The real vessel profiles are adopted for each week of data. After applying the selection cuts to this hybrid dataset we find the dead time fraction to be 27.6%. $^{214}$Bi-Po cut is the only cut which does not depend on muons, however it does not introduce any relevant dead time due to the extremely low rate. The residual detector livetime, after deadtime subtraction, is 1494 live days.

The rate of candidate events emerging from the selection cuts is 4.02 cpd. Untagged muons elude these cuts and could induce bursts of cosmogenic isotopes. To suppress this source of background we require a minimum time difference of 5 s between events. The expected number of random coincidences in a 5 s window is 1.4 in the whole data set, corresponding to an additional dead time fraction of $2.5\times10^{-4}$. A total of 17 events is rejected by this cut.

The final sample comprises of 6065 candidate events surviving all selection cuts, with an exposure of 1089±21 t·y after dead time subtraction. The resulting energy spectrum is shown in Figure 3 for both LE and HE energy windows. Residual background rates, after selection cuts, are listed in table I.

## V. UNTAGGED BACKGROUNDS

In this section we report on strategies developed to characterize backgrounds that survive selection cuts and cannot be identified on an event-by-event basis. Four sources of background are of this kind. Two of them, bulk $^{208}$Tl and *in situ* produced cosmogenic $^{11}$Be, are uniformly distributed within the scintillator volume. Another is represented by decays of $^{208}$Tl embedded in the

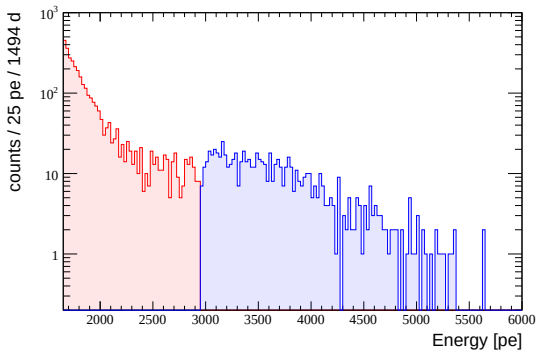


FIG. 3. Energy spectrum of residual events after selection cuts in the LE (red) and HE (blue) ranges. A z-cut at 2.5 m is applied to the LE region (see text) causing the step in the number of selected events visible at 2950 pe. No events are found in the HE sub-range [6000, 8500] p.e..

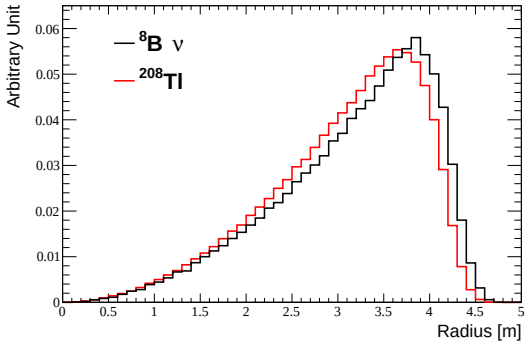


FIG. 4. Radial distributions of simulated $^8$B $\nu$ events and $^{208}$Tl decays, with [1650, 2950] p.e. energy cut. The two spectra are normalized to the number of reconstructed events. The difference is due to $^{208}$Tl emission $\gamma$-rays, escaping the scintillator.

nylon vessel or on its surface, and the last, *i.e.* high energy $\gamma$-rays from neutron captures on peripheral detector components, are external to the IV.

### A. $^{208}$Tl contamination

$^{208}$Tl, the product of $^{212}$Bi decays with 36% branching ratio, $\beta$-decays with $Q = 5.0$ MeV and the emission of both a $\beta$ and $\gamma$-rays. The $^{208}$Tl activity is quantified by looking at the alternative $^{212}$Bi decay mode (64% BR) and counting the $^{212}$Bi-$^{212}$Po delayed coincidences. The short mean life ($\tau = 431$ ns) of $^{212}$Po together with the space correlation between the two decays, makes these coincidences easy to identify with little to no background, allowing for an accurate estimation of $^{212}$Bi, and hence of $^{208}$Tl. For the latter we measure an activity of $(1.8\pm0.3)\times10^{-2}$ cpd/100 t. This is about 5 times lower than in earlier work [19], a consequence of the scintillator purification campaign occurred after the former search.

In the outermost shell of scintillator, 2.6 MeV $\gamma$-rays from $^{208}$Tl decays (99% BR) may escape into the buffer and shift the reconstructed event energy below the analysis threshold. This artificially shifts the radial distribution towards lower radii with respect to the neutrino induced electron recoils, as shown in Figure 4. For this reason, $^{208}$Tl is included as a separate component in the radial fit, carrying a penalty factor derived from the uncertainty on its measured bulk activity. This represents a difference with respect to the previous analysis, where $^{208}$Tl background was statistically subtracted from the total event rate.

### B. Cosmogenic $^{11}$Be

$^{11}$Be is a $\beta$ emitter with $Q = 11.5$ MeV and $\tau \sim 20$ s. In Borexino it is a product of muon spallation on $^{12}$C. *In situ* $^{11}$Be production in liquid scintillator was observed by KamLAND at the Kamioka mine [35], where the mean muon energy $\langle E_\mu \rangle \sim 260$ GeV. On the contrary, both Borexino (at Gran Sasso $\langle E_\mu \rangle \sim 280$ GeV) and the NA54 experiment at CERN, which investigated the production rate of radioactive isotopes in liquid scintillator with a muon beam (at 100 and 190 GeV) [36], were only able to set upper limits on the production of $^{11}$Be.

Our previous $^8$B analysis relied on the extrapolation of the $^{11}$Be rate from the KamLAND measurement, yielding $(3.2\pm0.6)\times10^{-2}$ cpd/100 t above 3 MeV. The new Borexino estimation of the $^{11}$Be rate is based on a larger exposure and on a multivariate fit that includes the energy spectrum and the time profile of events with respect to the preceding muon.

Candidate $^{11}$Be events are selected with $E > 6$ MeV from a [10, 150] s time window following the preceding muon. The lower time cut is set at 10 s to exclude events from other cosmogenic isotopes. To contain accidental background, the energy deposited by preceding muons must be larger than 5 MeV, and the $^{11}$Be candidate must be spatially confined within a 2 m radius from the muon track. The efficiency of the latter cut is >91.4%, obtained by assuming that all $^{11}$Be isotopes are produced by neutron spallation via $^{12}$C(n,2p)$^{11}$Be reaction by neutrons with an average lateral distance of 81.4 cm from the muon track, as measured in [33]. The assumption is conservative when considering that neutrons have the longest range of all muon-induced secondaries responsible of $^{11}$Be production, such as $\pi^-$, via $^{12}$C($\pi^-$,p)$^{11}$Be [37], and $^7$Li, via $^{12}$C($^7$Li,$^8$B)$^{11}$Be.

Events collected in the [150, 300] s window after a muon and occurring more than 2 m away from the muon track are used to evaluate accidental background.

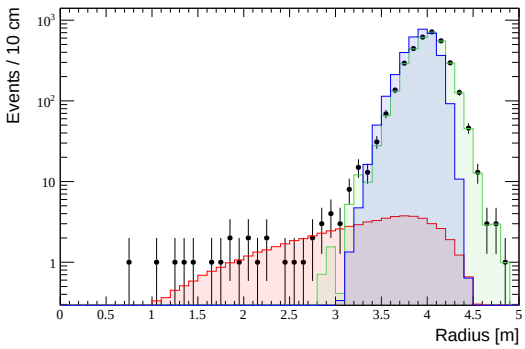


FIG. 5. Radial distributions of $^{212}$Bi events occurring in the scintillator, selected with the fast $^{212}$BiPo coincidences, with no energy degradation for the $\alpha$ decay (black dots). A uniform bulk distribution of simulated $^{212}$Bi events is shown in red. The difference (green) between the two spectra corresponds to $^{212}$Bi events resulting from emanation and diffusion from the nylon vessel. The distribution of *emanation* $^{208}$Tl is shown in blue. The $^{212}$Bi distribution (mostly a pure $\beta$ decay, $Q = 2.25$ MeV) is wider than that of $^{208}$Tl ($\beta + \gamma$ decay, $Q = 5$ MeV) due to poorer spatial resolution at lower energy. See text for details.

The $^{11}$Be spectral shape is obtained with Monte Carlo simulations, while the decay time profile is analytically modeled. The multivariate fit prefers a negative $^{11}$Be rate, and is compatible with zero. When setting a boundary condition requiring only null or positive rates, the fit results a $^{11}$Be rate above 3 MeV of zero with a positive sigma of $9.1\times10^{-3}$ cpd/100 t. This is $\sim$3 $\sigma$ lower than the rate extrapolated from the KamLAND measurement. The observed low rate may be due to the *cosmogenic* and $^{10}C$ cuts, which affects also $^{11}$Be events. The $^{11}$Be rates in the LE and HE ranges are listed in table I.

### C. Surface contamination

The nylon of the IV is the only material in direct contact with the scintillator, in addition to the plumbing of the filling and purification system. The IV was designed and constructed to make it as radio-pure as possible. The measured $^{238}$U and $^{232}$Th concentration in nylon is 5 and 20 ppt, respectively [38]. Nonetheless, while one of the cleanest solid materials ever assayed at the time Borexino was commissioned, its intrinsic radioactivity still exceeds that of the scintillator by many orders of magnitude. Events from the nylon vessel thus contribute to the event rate in the outermost shells of scintillator and call for volume fiducialization for most analyses.

The only vessel background causing events in the energy range of interest for this analysis is $^{208}$Tl, a daughter of $^{232}$Th embedded in the material. When it decays, $^{208}$Tl may find itself within the nylon membrane (contributing to what we call *surface* events), or in the fluid in close proximity of the vessel. Two mechanism can cause $^{208}$Tl to leave the nylon. Firstly, nuclei in the $^{232}$Th decay chain may recoil into the liquid as a result of one of the intermediate decays. Alternatively, $^{220}$Rn, a volatile progenitor of $^{208}$Tl can diffuse out of the nylon into the scintillator during its 56 s half life. Surface and *emanation* components display different spatial distributions, which we model independently.

Surface events are simulated by generating $^{208}$Tl decays uniformly across the nylon membrane. The emanated component cannot be reliably modeled because of the uncertainty introduced by convective motions of the scintillator [39]. The time delay between the appearance of $^{220}$Rn and the $^{208}$Tl decay is dominated by $^{212}$Pb ($\tau$ $\sim$15 hr). The diffusion scale of $^{208}$Tl over this time interval suggests that it may decay several cm from the vessel surface, a visible effect in Borexino.

The radial distribution of emanated $^{208}$Tl events is derived from the measured distribution of $^{212}$Bi-$^{212}$Po fast coincidences. When $\alpha$'s are emitted from $^{212}$Po implanted into the vessel, they lose a fraction of their energy inside the nylon and their scintillation signal appears degraded. Surface events can thus be discarded by selecting $^{212}$Po decays with full $\alpha$ energy deposition in scintillator. To extract the $^{212}$Bi emanation component from the distribution of $^{212}$Bi-$^{212}$Po events, bulk $^{212}$Bi events are simulated and subtracted from the $^{212}$Bi data sample, after being normalized by their intrinsic contamination measured in the scintillator (see Figure 5).

Despite $^{212}$Bi and $^{208}$Tl being equally located in space, their distributions differ because of energy-dependent resolution effects. We derive the true "emanated" $^{212}$Bi radial distribution using the ROOT TSpectrum *deconvolution* algorithm [40] to deconvolve the detector response. The difference between reconstructed and true radius for events generated 1 cm away from the vessel inside the scintillator is obtained from Monte Carlo simulation. The true radial distribution is in turn convolved with the Monte Carlo spatial response function generated for $^{208}$Tl events, with the same procedure used for $^{212}$Bi. The final $^{208}$Tl radial distribution is shown in Figure 5.

The surface and emanation radial distributions of $^{208}$Tl are included in the fitting strategy, described in Section VI. Uncertainties on the detector spatial response for both $^{212}$Bi and $^{208}$Tl events are included in the evaluation of systematic uncertainties, as discussed in Section VI.

### D. Radiogenic neutron captures

The HE data sample should only contain bulk scintillator events, namely $^{8}$B neutrinos and cosmogenic $^{11}$Be. No contributions from long-lived, natural radioactivity with E>5 MeV is expected. However, the data show an excess of events at large radii at odds with a bulk distribution, as shown in Figure 6. This effect was not previously observed because of limited statistics.

The excess can be explained by $\gamma$-rays arising from

TABLE II. $^{238}$U, $^{235}$U, and $^{232}$Th contaminations in stainless steel and PMT glass from Borexino material screening measurements [38], assuming secular equilibrium; neutron fluxes from ($\alpha$, n) reactions and fissions.

| | SSS (45 t) | | | PMT Glass (1.77 t) | | |
|---|---|---|---|---|---|---|
| | $^{238}$U | $^{235}$U | $^{232}$Th | $^{238}$U | $^{235}$U | $^{232}$Th |
| Concentration [g/g] [38] | 3.7 $10^{-10}$ | 2.7 $10^{-12}$ | 2.8 $10^{-9}$ | 6.6 $10^{-8}$ | 4.8 $10^{-10}$ | 3.2 $10^{-8}$ |
| ($\alpha$, n) rate [n/decay] [41] | 5.0 $10^{-7}$ | 3.8 $10^{-7}$ | 1.9 $10^{-6}$ | 1.6 $10^{-5}$ | 1.9 $10^{-5}$ | 1.8 $10^{-5}$ |
| ($\alpha$, n) neutron flux [year$^{-1}$] | 3.3 $10^{3}$ | 1.2 $10^{2}$ | 3.1 $10^{4}$ | 7.3 $10^{5}$ | 4.1 $10^{4}$ | 1.3 $10^{5}$ |
| Spontaneous fission rate [n/(g s)][42] | 1.36 $10^{-2}$ | 3.0 $10^{-4}$ | <1.32 $10^{-7}$ | 1.36 $10^{-2}$ | 3.0 $10^{-4}$ | <1.32 $10^{-7}$ |
| Spontaneous fission neutron flux [year$^{-1}$] | 7.1 $10^{4}$ | O(< 1) | O(< 1) | 5.0 $10^{2}$ | O(< 1) | O(< 1) |

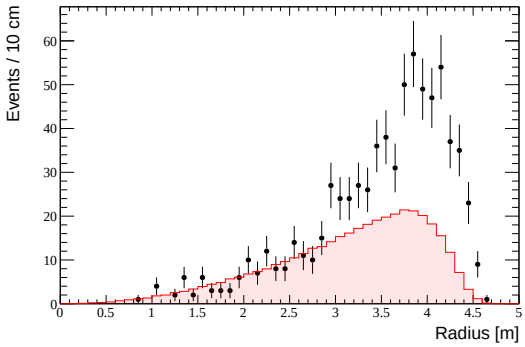


FIG. 6. Radial distribution of $^{8}$B candidates (black dots) compared with the Monte Carlo (red) one for events with Q>2950 pe (∼5MeV). The excess at large radii is an indication for the additional high energy external background component induced by radiogenic neutron captures on detector materials.

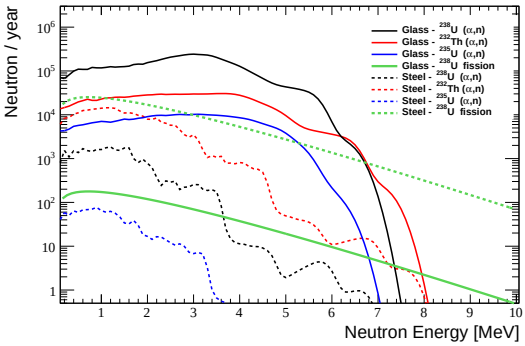


FIG. 7. Predicted energy spectra and fluxes of neutrons produced via ($\alpha$, n) reactions and spontaneous fissions, from $^{238}$U, $^{235}$U, and $^{232}$Th contaminations in SSS and in PMT glasses.

the capture of radiogenic neutrons produced in detector materials via ($\alpha$, n) or spontaneous fission reactions. Two sufficiently massive detector components with non-negligible $^{238}$U, $^{235}$U, and $^{232}$Th contamination are identified as possible sources of neutrons: the ∼45 t SSS, and the glass of the PMT's (totaling ∼0.8 kg × 2212 PMT's ∼1.77 t).

The $^{238}$U and $^{232}$Th contamination of the SSS and the PMT glass measured by the Borexino [38] are reproduced in table II. The $^{235}$U contamination is obtained from $^{238}$U imposing the natural isotopic ratio, and the neutron yield used in this study assumes secular equilibrium along each decay chain. Some Borexino detector components, such as the PMT dynode structure, are known to have a higher specific radioactive contamination, but are neglected here in light of their limited total mass.

The mean number of ($\alpha$, n) neutrons per decay and their associated energy spectra in each material are evaluated for each decay chain with NEUCBOT [43], a tool based on the TALYS simulation package [41] that also accounts for any $\alpha$ energy lost inside materials.

The energy spectrum of neutrons produced by spontaneous fission reactions is modeled with the Watt's semi-empirical relation [44], as

$$f(E) \propto \mathrm{Sinh}(\sqrt{2E})\, e^{-E}, \qquad (1)$$

The corresponding neutron fluxes are derived from reference [42] and quoted in table II.

Neutrons emerging from the SSS and the PMT glass are simulated with the Borexino Monte Carlo framework [32], using the input energy distributions described above (Fig. 7 and Eq. 1). The simulation indicates that neutrons capture mainly on the iron of the SSS and on the hydrogen and carbon in the buffer fluid within ∼80 cm of the SSS, producing $\gamma$-rays with energies up to ∼10 MeV. These $\gamma$-rays are attenuated by the remaining ∼2 m-thick buffer fluid separating it from the scintillator volume. The fraction of events with $E > 1650$ p.e. ranges between $10^{-5}$ and $10^{-4}$, depending on the location of the neutron capture and the energy of the emitted $\gamma$-ray. The simulations of energetic $\gamma$-rays from the detector periphery were validated in Borexino with the deployment of a $^{228}$Th calibration source [32].

We calculate that 148 (151) events induced by neutrons in the LE (HE) data samples. The uncertainty on this estimation is dominated by the ($\alpha$, n) cross sections. As discussed in [43], disagreement of up to 100% exists between data compilations and predictions by TALYS and

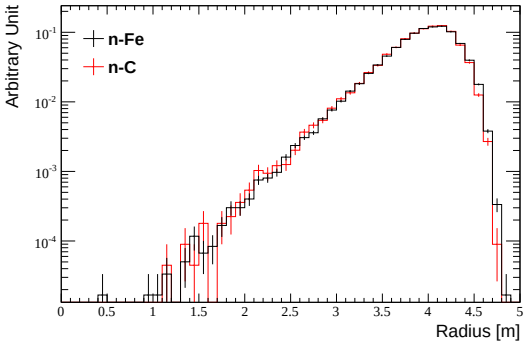


FIG. 8. Reconstructed radial distributions of simulated events with energy falling in the LE range and generated by neutron captures on carbon in the buffer (red), and on iron in the SSS (black).

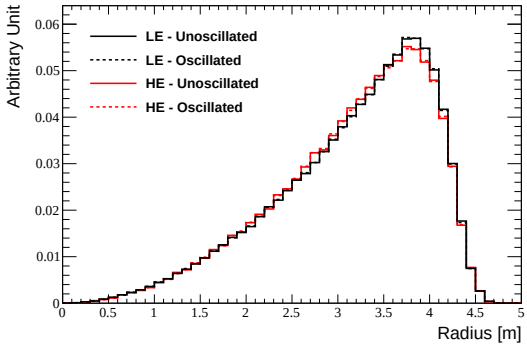


FIG. 9. Comparison of the radial distributions from unoscillated and oscillated neutrinos in the LE and HE ranges. Oscillated and unoscillated spectra are almost indistinguishable, confirming the negligible dependence of the radial distribution on the energy spectrum. The MSW-LMA parameters used for simulating oscillating neutrinos are $\Delta m^2$=7.50×10$^{-5}$ eV$^2$, $\sin^2(\theta_{12})$=0.306, and $\sin^2(\theta_{13})$=0.02166 [47].

SOURCES-4C [45], an alternative code for calculating $\alpha$-induced neutron fluxes. In the same reference, good agreement between the predicted neutron energy spectra is reported.

We finally address possible systematic effects on the reconstructed radial distribution of events in the LE range. These arise from a possible imbalance between $\gamma$-rays produced in the buffer region and in the SSS and PMTs caused by a simplified model of the detector used in the simulations, which lacks certain details such as, *e.g.*, the internal PMT structure and the cable feedthroughs. We compare the distribution of events from neutron captures in the buffer and in the SSS and observe minor differences limited to the vessel edge, as shown in Figure 8. The impact of this systematic is evaluated in the next section.

## VI. DATA ANALYSIS

The identification of the neutrino signal relies on its different radial distribution from that of background. Neutrino candidates are expected to be uniformly distributed throughout the scintillator, a property shared with $^{11}$Be background that is described by the same radial function but whose rate is, however, constrained as illustrated in Section V. The *bulk* $^{208}$Tl on the contrary, follows a different distribution, as shown in Fig. 4 and discussed in Section V.

The $^8$B energy spectrum used here is that from W. Winter *et al.* [46]. Spectral distortions due to neutrino flavor conversion have no impact on the shape of the radial LE and HE distributions, as illustrated in Figure 9, where radial shapes simulated for both energy windows with and without MSW-LMA flavor conversion are compared.

The radial fit estimator is the binned likelihood ratio, to account for empty bins at small radii. We include a penalty factor constraining the bulk $^{208}$Tl component to the known uncertainty on its rate.

TABLE III. LE and HE rates of signal and background components from the radial distribution fits (only statistical errors are quoted). Bulk events are dominated by $^8$B neutrinos, with contributions from $^{11}$Be decays and residual background quoted in Tab. I

| Component | LE rate [cpd/227.8 t] | HE rate [cpd/266.0 t] |
|---|---|---|
| Bulk events | 0.310±0.029 | 0.235±0.021 |
| External | 0.224±0.078 | 0.239±0.022 |
| $^{208}$Tl bulk | 0.042±0.008 | - |
| $^{208}$Tl emanation | 0.469±0.063 | - |
| $^{208}$Tl surface | 1.090±0.046 | - |

The HE data sample is fitted with 2 components only: $^8$B neutrinos and the external component from neutron captures. The LE sample requires three additional fit components, all due to $^{208}$Tl: *bulk* (dissolved in the scintillator), *surface* (intrinsic to the nylon vessel), and *emanation* (diffused from the nylon vessel into the outer edge of scintillator). The fit results are summarized in table III.

The HE and LE radial fits are shown in Fig. 10 and Fig. 11, and the corresponding $\chi^2$/dof, excluding empty bins, of 30.4/35 (HE) and 31.3/36 (LE). The *emanation* $^{208}$Tl rate is measured at 0.47±0.06 cpd. It is worth mentioning that its exclusion from the LE fit leads to a $\chi^2$/dof of 91.6/36.

The number of external neutron capture-induced events from the fit is 351±31 and 335±117 for the HE and LE ranges, respectively. In both cases the best-fit number is ∼2 times larger than predicted by simulations, still within less than 2 $\sigma$, including model uncertainties.

The best-fit normalization of the *bulk* $^{208}$Tl component for the LE dataset is close to the central value expected

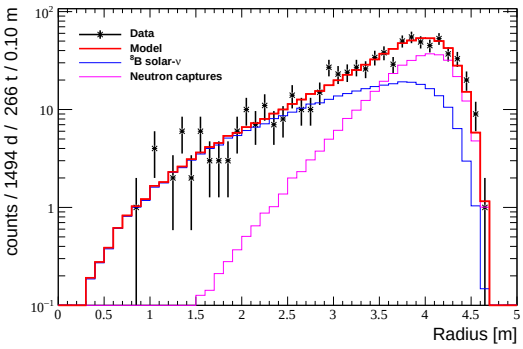


FIG. 10. Fit of the event radial distribution in the HE range, [2950, 8500] p.e..

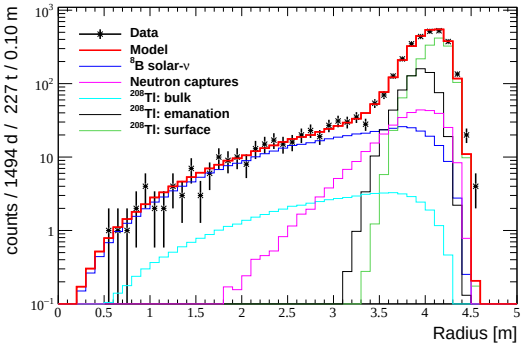


FIG. 11. Fit of the event radial distribution in the LE range, [1650, 2950] p.e..

from the rate of $^{212}$BiPo coincidences. The weak anti-correlation coefficient (−0.299) between $^8$B neutrinos and $^{208}$Tl substantiates the ability of the fit to discriminate between these two distributions.

The best-fit rate of $^8$B neutrinos, after subtraction of residual backgrounds itemized in table III, is 0.133±0.013 cpd/100 t for the LE energy range and $0.087^{+0.008}_{-0.010}$ cpd/100 t for the HE window. The total rate above 1650 p.e. is $0.220^{+0.015}_{-0.016}$ cpd/100 t.

The result from the fit is stable (within 1 $\sigma_{stat}$) to changes of the histogram binning and to a ±3% linear distortion of the simulated radius. A slight decrease in the normalized $\chi^2$ was observed by multiplying the simulated radius by 1.015, improving the agreement at large radii, small enough to raise any issue with the radius in the model.

The fitted $^8$B neutrino interaction rates were tested to be stable to changes of the response function used for deconvolving (convolving) the $^{212}$Bi ($^{208}$Tl) spatial distribution, determining the radial profile of the *emanation* $^{208}$Tl component (see Fig. 5). Its stability was specifically tested with a response function simulating events located 6 cm away from the IV, inside the scintillator, and no appreciable effect was observed.

Finally, we tested the fit stability against variations of the radial shape of the neutron capture γ-rays component, assuming the limiting cases of neutrons exclusively capturing on the SSS or the buffer fluid, shown in Figure 8. A smaller normalized $\chi^2$ is obtained when considering neutron captures on SSS only, but the $^8$B neutrino rate is stable within statistical uncertainty.

The systematic sources mostly affecting the result are the determination of the active mass and the uncertainty on the energy scale (both discussed in section IV), and the z-cut applied in the LE range. To quantify the effect of the latter, we performed the fit with a modified z-cut, ±0.5 m around the chosen value (2.5 m). The other systematic effects were evaluated with Monte Carlo simulations. Subdominant sources of systematic uncertainty relate to the scintillator density and to the live time estimation. Systematic uncertainties for the LE and HE ranges are collected in Table IV.

TABLE IV. Systematic sources and percentage uncertainties of the measured rates in the LE, HE, and LE+HE ranges.

| | LE | HE | LE+HE |
|---|---|---|---|
| Source | $\sigma$ | $\sigma$ | $\sigma$ |
| Active mass | 2.0 | 2.0 | 2.0 |
| Energy scale | 0.5 | 4.9 | 1.7 |
| z-cut | 0.7 | 0.0 | 0.4 |
| Live time | 0.05 | 0.05 | 0.05 |
| Scintillator density | 0.5 | 0.5 | 0.5 |
| Total | 2.2 | 5.3 | 2.7 |

In summary, the final $^8$B solar neutrino rates in the LE, HE, and combined energy regions are:

$$R_{LE} = 0.133^{+0.013}_{-0.013}\,(stat)\,^{+0.003}_{-0.003}\,(syst)\ \text{cpd/100 t},$$

$$R_{HE} = 0.087\,^{+0.08}_{-0.010}\,(stat)\,^{+0.005}_{-0.005}\,(syst)\ \text{cpd/100 t},$$

$$R_{LE+HE} = 0.220^{+0.015}_{-0.016}\,(stat)\,^{+0.006}_{-0.006}\,(syst)\ \text{cpd/100 t}.$$

The precision on the LE+HE $^8$B rate measurement is ∼8%, improved by more than a factor 2 with respect to our previous result [19].

## VII. $^8$B NEUTRINO FLUX AND SURVIVAL PROBABILITY

The measured $^8$B solar neutrino rate in the LE+HE range is in good agreement with 0.211±0.025 cpd/100t, *i.e.* that expected from the B16 SSM [24] with high metallicity (GS98 [27]), and assuming MSW+LMA flavor transformation. The equivalent flavor-stable $^8$B neutrino flux inferred from this measurement is $2.55^{+0.17}_{-0.19}(stat)^{+0.07}_{-0.07}(syst)\times10^6$ cm$^{-2}$s$^{-1}$, in good agreement with the previous Borexino result of 2.4±0.4×10$^6$ cm$^{-2}$s$^{-1}$ [19] and with the high-precision measurement by SuperKamiokande, 2.345±0.014($stat$)±0.036($syst$)×10$^6$ cm$^{-2}$ s$^{-1}$ [14]).

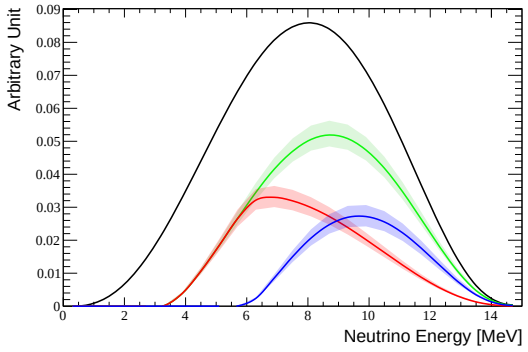


FIG. 12. The $^8$B neutrino energy spectrum (black) and the portions of the same spectrum contributing to the LE (red), HE (blue), and LE+HE (green) energy windows used in this analysis. No flavor transformation is assumed. The error bands are obtained by combining statistical and systematic uncertainties of the measured rates.

Figure 12 shows the fraction of the $^8$B neutrino spectrum generating scattered electrons falling in the LE, HE, and combined LE+HE ranges. The corresponding neutrino mean energies are 7.9 MeV, 9.9 MeV, and 8.7 MeV respectively.

For each range, we calculate the average electron neutrino survival probability, $\bar{P}_{ee}$, according to the MSW-LMA model and following the same procedure used in [19]. This is shown, together with $\bar{P}_{ee}$ for other solar neutrino sources, in Figure 13. We find $\bar{P}_{ee}$ in the LE+HE range, including the uncertainty on the solar neutrino flux, equal to 0.36±0.08, in good agreement with the expected value (0.335±0.008). The $^8$B neutrino rates for the LE and HE ranges are fully compatible (albeit with weak discrimination power) with the presence of an "upturn" of $\bar{P}_{ee}$ in the transition region between matter and vacuum flavor conversion predicted by MSW-LMA.

It is interesting to alternatively consider the low metallicity solar model AGSS09met [26], which predicts almost identical (to the percent level) *pp* and *pep* neutrino fluxes and significantly reduced $^7$Be and $^8$B neutrino fluxes by ∼18% with respect to high metallicity models. Figure 14 shows $\bar{P}_{ee}$ for the low-Z case. The average electron neutrino survival probability for the LE+HE $^8$B solar neutrino increases in this case to 0.479±0.09. The ensemble of solar neutrino measurements by Borexino show some tension with low-Z solar models.

The combination of solar neutrino measurements by Borexino ($^8$B from this work, *pp* and $^7$Be from [28]), by SuperKamiokande [14] and by SNO [20] prefers the high-Z solar model at ∼2 $\sigma$ ($p$-value = 0.956), while it is less compatible with the low-Z model (∼0.6 $\sigma$, $p$-value = 0.465). Using Borexino data only, the high-Z solar model is preferred at 3.1 $\sigma$, while the low-Z one is compatible at 0.3 $\sigma$ only. The discrimination between the two models solely based on $^8$B, *pp*, and $^7$Be neutrino rates is limited by SSM uncertainties. It is noteworthy that a measurement of CNO solar neutrinos with 10-15% precision, whose flux predictions vary by ∼30% between high-Z and low-Z models, has the potential to definitively settle the solar metallicity controversy.

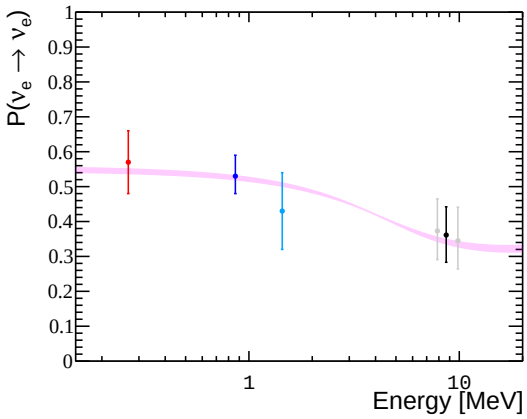


FIG. 13. Electron neutrino survival probability as function of the neutrino energy, evaluated for the $^8$B neutrino source assuming the high-Z B16(GS98) SSM [24, 27] and the flavor conversion parameters from the MSW-LMA solution ($\Delta m^2_{12}$=7.50×10$^{-5}$ eV$^2$, $\tan^2\theta_{12}$=0.441, and $\tan^2\theta_{13}$=0.022 [47]). Dots represent the Borexino results from *pp* (red), $^7$Be (blue), *pep* (azure), and $^8$B neutrino measurements (black for the LE+HE range, and grey for the separate sub-ranges). *pp* and $^8$B dots are set at the mean energy of detected neutrinos, weighted on the detection range in electron recoil energy. The error bars include experimental and theoretical uncertainties.

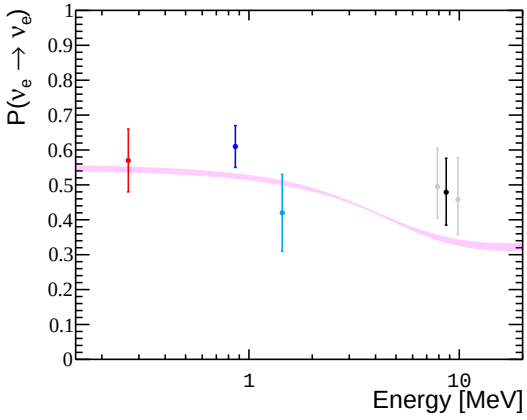


FIG. 14. Electron neutrino survival probability as function of the neutrino energy and Borexino measurements, assuming the low-Z B16(AGSS09met) SSM [24, 26]. Color codes and explanation are the same of Figure 13.

## VIII. CONCLUSIONS

In this work, we report on a new measurement of the $^8$B solar neutrino rate with Borexino, obtained with ∼1.5 kt·y of exposure, ∼11.5 times the statistics used in the previous analysis [19].

Key improvements from the previous measurement include a lower $^{208}$Tl contamination in the purified scintillator, the addition of radiogenic neutron captures on detector components to the detector background model, and a tighter constraint set on the rate of cosmogenic $^{11}$Be. Just as importantly, the analysis rests on a greatly improved detector Monte Carlo simulation package, able to model data at percent level. As a consequence, the analysis was extended to include the entire scintillator volume and the uncertainty of the $^8$B rate was reduced from ∼19% to ∼8%.

This measurement complements the recent work on the simultaneous spectroscopy of *pp*, $^7$Be, and *pep* solar neutrinos with Borexino Phase-II data [28].

## ACKNOWLEDGMENTS

The Borexino program is made possible by funding from INFN (Italy), NSF (USA), BMBF, DFG, HGF, and MPG (Germany), RFBR (Grants 16-02-01026 A, 15-02-02117 A, 16-29-13014 ofim, 17-02-00305 A) (Russia), and NCN (Grant No. UMO 2013/10/E/ST2/00180) (Poland). We acknowledge the generous hospitality and support of the Laboratory Nazionali del Gran Sasso (Italy).

[1] B. Cleveland, T. Daily, R. Davis Jr, J. Distel, K. Lande, C. Lee, P. Wildenhain, and J. Ullman, The Astrophysical Journal **496**, 505 (1998).
[2] K. S. Hirata *et al.* (Kamiokande-II), Phys. Rev. Lett. **63**, 16 (1989).
[3] J. N. Abdurashitov *et al.* (SAGE), Phys. Rev. **C60**, 055801 (1999), arXiv:astro-ph/9907113 [astro-ph].
[4] W. Hampel *et al.* (GALLEX), Phys. Lett. **B447**, 127 (1999).
[5] M. Altmann *et al.* (GNO), Phys. Lett. **B616**, 174 (2005), arXiv:hep-ex/0504037 [hep-ex].
[6] K. Abe *et al.* (Super-Kamiokande Collaboration), Phys. Rev. D **94**, 052010 (2016).
[7] Q. R. Ahmad *et al.* (SNO), Phys. Rev. Lett. **89**, 011301 (2002), arXiv:nucl-ex/0204008 [nucl-ex].
[8] S. P. Mikheev and A. Yu. Smirnov, Sov. J. Nucl. Phys. **42**, 913 (1985), [Yad. Fiz.42,1441(1985)].
[9] L. Wolfenstein, Phys. Rev. **D17**, 2369 (1978).
[10] T. Kajita, Rev. Mod. Phys. **88**, 030501 (2016).
[11] G. J. Feldman, J. Hartnell, and T. Kobayashi, Adv. High Energy Phys. **2013**, 475749 (2013), arXiv:1210.1778 [hep-ex].
[12] C. Mariani, Mod. Phys. Lett. **A27**, 1230010 (2012), arXiv:1201.6665 [hep-ex].
[13] K. Eguchi *et al.* (KamLAND), Phys. Rev. Lett. **90**, 021802 (2003), arXiv:hep-ex/0212021 [hep-ex].
[14] K. Abe *et al.* (Super-Kamiokande), Phys. Rev. **D94**, 052010 (2016), arXiv:1606.07538 [hep-ex].
[15] C. Arpesella *et al.* (Borexino), Phys. Rev. Lett. **101**, 091302 (2008), arXiv:0805.3843 [astro-ph].
[16] G. Bellini *et al.* (Borexino), Phys. Rev. Lett. **108**, 051302 (2012), arXiv:1110.3230 [hep-ex].
[17] G. Bellini *et al.* (Borexino), Nature **512**, 383 (2014).
[18] G. Bellini *et al.* (Borexino), Phys. Rev. **D89**, 112007 (2014), arXiv:1308.0443 [hep-ex].
[19] G. Bellini *et al.* (Borexino), Phys. Rev. **D82**, 033006 (2010), arXiv:0808.2868 [astro-ph].
[20] B. Aharmim *et al.* (SNO), Phys. Rev. **C88**, 025501 (2013), arXiv:1109.0763 [nucl-ex].
[21] H. Minakata and C. Pena-Garay, Adv. High Energy Phys. **2012**, 349686 (2012), arXiv:1009.4869 [hep-ph].
[22] P. C. de Holanda and A. Y. Smirnov, Phys. Rev. D **69**, 113002 (2004).
[23] P. C. de Holanda and A. Yu. Smirnov, Phys. Rev. **D83**, 113011 (2011), arXiv:1012.5627 [hep-ph].
[24] N. Vinyoles, A. M. Serenelli, F. L. Villante, S. Basu, J. Bergström, M. C. Gonzalez-Garcia, M. Maltoni, C. Peña-Garay, and N. Song, Astrophys. J. **835**, 202 (2017), arXiv:1611.09867 [astro-ph.SR].
[25] S. Basu and H. M. Antia, Phys. Rept. **457**, 217 (2008), arXiv:0711.4590 [astro-ph].
[26] M. Asplund, N. Grevesse, A. J. Sauval, and P. Scott, Ann. Rev. Astron. Astrophys. **47**, 481 (2009), arXiv:0909.0948 [astro-ph.SR].
[27] N. Grevesse and A. Sauval, Space Science Reviews **85**, 161 (1998).
[28] M. Agostini *et al.* (Borexino), (2017), arXiv:1707.09279 [hep-ex].
[29] G. Bellini *et al.* (Borexino), JINST **6**, P05005 (2011), arXiv:1101.3101 [physics.ins-det].
[30] G. Alimonti *et al.* (Borexino), Nucl. Instrum. Meth. **A600**, 568 (2009), arXiv:0806.2400 [physics.ins-det].
[31] H. Back *et al.* (Borexino), JINST **7**, P10018 (2012), arXiv:1207.4816 [physics.ins-det].
[32] M. Agostini *et al.* (Borexino), (2017), arXiv:1704.02291 [physics.ins-det].
[33] G. Bellini *et al.* (Borexino), JCAP **1308**, 049 (2013), arXiv:1304.7381 [physics.ins-det].
[34] H. O. Back *et al.* (Borexino), Nucl. Instrum. Meth. **A584**, 98 (2008), arXiv:0705.0239 [physics.ins-det].
[35] S. Abe *et al.* (KamLAND), Phys. Rev. C **81**, 025807 (2010).
[36] T. Hagner, R. von Hentig, B. Heisinger, L. Oberauer, S. Schoenert, F. von Feilitzsch, and E. Nolte, Astroparticle Physics **14**, 33 (2000).
[37] C. Galbiati, A. Pocar, D. Franco, A. Ianni, L. Cadonati, and S. Schonert, Phys. Rev. **C71**, 055805 (2005), arXiv:hep-ph/0411002 [hep-ph].
[38] C. Arpesella *et al.* (Borexino), Astropart. Phys. **18**, 1 (2002), arXiv:hep-ex/0109031 [hep-ex].
[39] D. Bravo-Berguo, R. Mereu, R. B. Vogelaar, and F. Inzoli, (2017), arXiv:1705.09658 [physics.ins-det].

[40] R. Brun and F. Rademakers, *New computing techniques in physics research V. Proceedings, 5th International Workshop, AIHENP '96, Lausanne, Switzerland, September 2-6, 1996*, Nucl. Instrum. Meth. **A389**, 81 (1997).
[41] A. J. Koning, S. Hilaire, and M. Duijvestijn, Proceedings of the International Conference on Nuclear Data for Science and Technology, April 22-27, 2007, Nice, France , 211 (2008).
[42] H. Smith, N. Ensslin, and D. Reilly, "Passive nondestructive assay of nuclear materials," (1991), 339 pp.
[43] S. Westerdale and P. D. Meyers, (2017), arXiv:1702.02465 [physics.ins-det].
[44] D. B. Nicodemus and H. H. Staub, *Fission Neutron Spectrum of* $^{235}U$, Vol. 89 (American Physical Society, 1953) pp. 1288–1290.
[45] E. Shores, Nuclear Instruments and Methods in Physics Research Section B: Beam Interactions with Materials and Atoms **179**, 78 (2001).
[46] W. T. Winter, S. J. Freedman, K. E. Rehm, and J. P. Schiffer, Phys. Rev. C **73**, 025503 (2006).
[47] I. Esteban, M. C. Gonzalez-Garcia, M. Maltoni, I. Martinez-Soler, and T. Schwetz, JHEP **01**, 087 (2017), arXiv:1611.01514 [hep-ph].